Int J Adv Manuf Technol (2016) 83:1917–1926
DOI 10.1007/s00170-015-7703-0

ORIGINAL ARTICLE

Effects of electrode tip morphology on resistance spot welding quality of DP590 dual-phase steel

Bin Wang [1,3] · **Lin Hua** [1,2] · **Xiaokai Wang** [1,2,3] · **Yuke Song** [1,3] · **Yali Liu** [1,3]

Received: 12 May 2015 / Accepted: 6 August 2015 / Published online: 21 August 2015

Abstract Electrode pitting (EP) and electrode tip diameter enlargement (ETDE) are the two major representations of electrode wear, which lead to the change of electrode tip morphology and have significant impacts on the resistance spot welding (RSW) quality. In order to analyze the effects of electrode tip morphology on RSW quality of DP590 dual-phase steel, the RSW finite element (FE) model is developed to predict the nugget shape and size, whose reliability is verified by experimental observation. Tensile-shear tests are carried out to illustrate the failure behaviors. Three nugget shapes and two failure modes are obtained from different conditions of electrode tip morphology. The results show that EP morphologies produce incomplete fusion at the center of the workpieces' faying surface, while ETDE morphologies reduce the nugget sizes. Both obvious EP and ETDE morphologies resulted in a decline of lap shear fracture load (LSFL).

Keywords Electrode pitting · Electrode tip diameter enlargement · Electrode tip morphology · Resistance spot welding · Dual-phase steel

✉ Xiaokai Wang
wxk0919@whut.edu.cn; wxk0919@163.com

[1] Hubei Key Laboratory of Advanced Technology for Automotive Components Wuhan, University of Technology, Wuhan 430070,, China

[2] Hubei Collaborative Innovation Center for Automotive Components Technology, Wuhan 430070, China

[3] School of Automotive Engineering, Wuhan University of Technology, Wuhan 430070, China

1 Introduction

In the automotive manufacturing industry, resistance spot welding (RSW) is the main connection technology. A car body typically contains thousands of spot welds. As lightweight of automobile becomes an inevitable trend with the rapid development of auto industry, the advanced high-strength steel (AHSS) like dual-phase (DP) steel is widely adopted to reduce the car's total weight. Many researches have been made on weldability, influence of welding parameters, process optimization, and mechanical performance in RSW of AHSS. Yang et al. [1] studied the weldability of DP600 sheet to cylindrical tube single-side spot welding through analysis of the dynamic resistance. Mohsen et al. [2] analyzed the main effects and interactions of the current intensity, welding time, sheet thickness, electrode face radius, and squeeze force over a realistic range of values. Hayat and Sevim [3] indicated that the welding time and welding current had great effects on the size and fracture toughness of the welded joint. Zhang et al. [4] revealed three failure modes of the dissimilar thickness DP600/DP780 joints.

A major problem in RSW is the short electrode life. It not only needs to replace or grind frequently, but also reduces productivity. The service life of the electrode in RSW of uncoated steels reached more than 10,000 welds. While there were less than 2000 welds in RSW of coated steels, there were 1000 welds in RSW of aluminum alloy [5, 6]. Zhang et al. [7] shown that there was no nugget formed at 1200 welds for welding DP600 steel. Electrode wear is the main factor that affects the service life of electrode, and it is hard to be controlled and will influence welding quality seriously [8]. Welding AHSS leads the electrode wear faster than uncoated steels. Plastic deformation and pitting are the major manifestations of electrode wear. Holliday et al. [9] stated that electrode would produce plastic deformation under the high

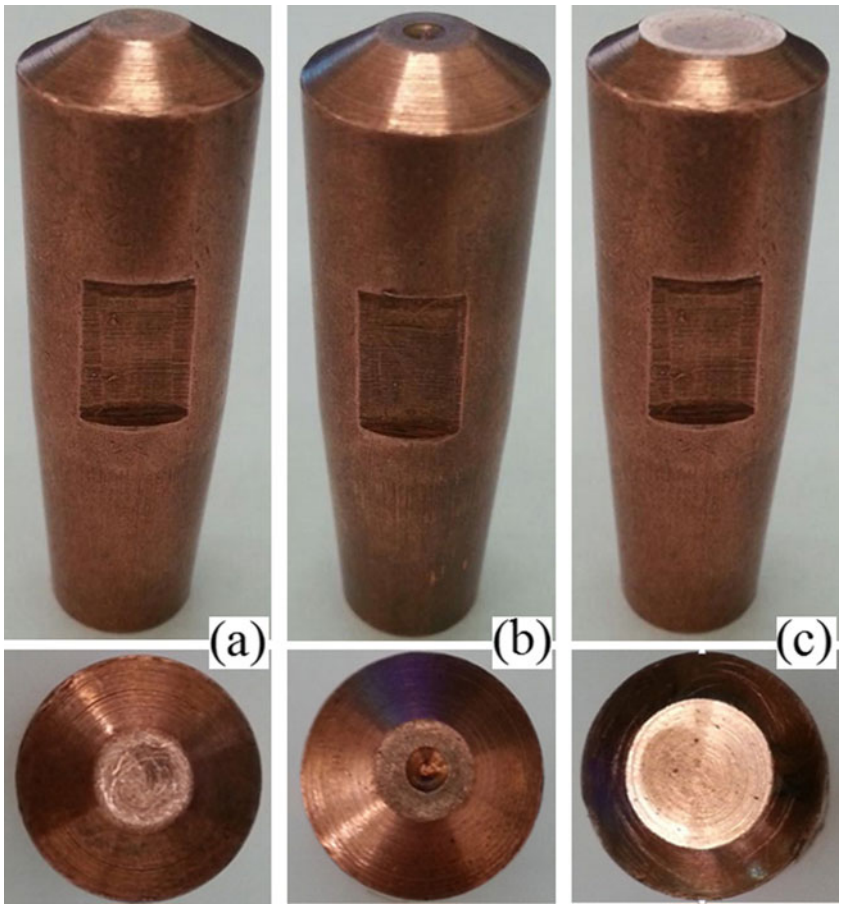

Fig. 1 Electrode tip morphologies: **a** normal, **b** EP, and **c** ETDE

temperature and pressure of RSW, which led to electrode tip diameter enlargement (ETDE). Lum et al. [10] illustrated that electrode pitting (EP) is a result of material removal from the electrode tip face.

RSW is a complicated process, involving interactions of electrical, thermal, mechanical, and metallurgical phenomena. Welding finite element (FE) simulation is an effective and reasonable method to study the RSW mechanism. Khan et al. [11] and Xu et al. [12] simulated the RSW process in ABAQUS and analyzed the melting nucleation process. Nodeh et al. [13] modeled welding residual stresses during different stages of RSW. Karimi et al. [14] developed a 2D coupled electrical-thermal and incrementally coupled thermal-mechanical FE model of RSW process of aluminum alloy 6061-T6. Ma and Murakawa [15] studied the nugget formation in RSW for three pieces of AHSS sheets.

Researches of electrode wear mainly concentrated on the electrode service life and electrode failure form [7, 16]. After welding a certain number of spot welds, there is no nugget formed because of electrode wear, and the electrode should be replaced or ground. But, the electrode tip morphology after wear, which has a significant impact on welding quality, is rarely studied at present. It is well known that nugget size and failure behavior are considered as the most important factors of welding quality assessment. So, in this paper, the FE modeling for RSW of DP590 steel under different electrode tip morphology was performed in ABAQUS software, and the nugget shape and size were investigated and validated against metallographic experiments. Also, the failure behaviors were investigated through the tensile-shear test considering the effects of electrode tip morphology.

Table 1 Chemical composition of DP590 steel (weight %)

C	Si	Mn	P	S	Alt
0.078	0.03	1.76	0.01	0.004	≥0.02

Table 2 Welding conditions (1 cycle is equal to 0.02 s)

Parameters	Values
Squeeze time (cycle)	20
Welding current (kA)	7.4
Welding time (cycle)	12
Electrode force (kN)	2.5
Cooling water volume (L/min)	12
Holding time (cycle)	25

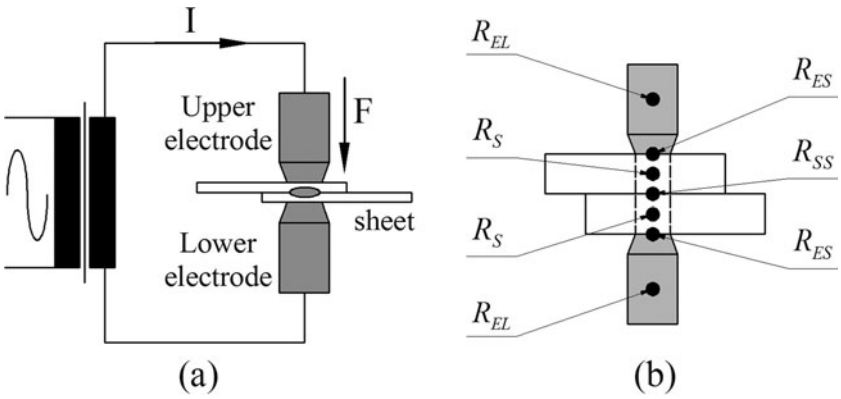

Fig. 2 **a** Principle of RSW. **b** The resistance of each part in RSW

2 Experimental preparation

Electrode wear occurs frequently in RSW of coated steels [17]. Coating metal tends to react with copper electrode during RSW under high temperature and pressure, which leads to the formation of alloy layer in electrode surface. Because of the poor electrical and thermal conductivity of these alloy layers, they are prone to adhesion and falling off from the electrode surface during weld process, even generating the plastic deformation, resulting in ETDE. The cause of EP is that after electrode leaving the workpiece, some low melting point alloys will leave electrode tip under the action of expulsion. Therefore, a small crater is produced on the electrode tip, and a lot of craters form EP. The morphologies of ETDE and EP are shown in Fig. 1. EP morphology was idealized as a small electrode concentric hole on electrode tip, taking the hole diameter instead of the pitting diameter. Similarly, ETDE morphology was manifested as the uniform increase of electrode tip diameter.

The 1-mm-thick DP steel DP590 was used as the base metals. The chemical composition of this steel is presented in Table 1. Two types of specimens with different sizes were selected in experiments. The 40×40-mm specimens were provided for metallographic experiments, and 100×30-mm specimens were for the tensile-shear test. RSW was carried out using a calibrated DN-35 kVA spot welding machine. The welding conditions are listed in Table 2.

The principle of RSW is shown in Fig. 2a. Two overlapped sheets are held together and under pressed between two columnar electrodes, then switched on the electrical current, using the resistance heat of sheets' contact surface to melt the part metals and form nugget. The resistance of each part in RSW is presented in Fig. 2b. The total resistance R and the heat generation Q can be calculated as follows:

$$R = R_{SS} + 2R_{ES} + 2R_S \quad (1)$$

$$Q = I^2Rt \quad (2)$$

where R_{SS} and R_{ES} are the contact resistance of sheet/sheet and electrode/sheet, respectively. R_S is the resistance of sheet, I is the welding current, and t is the welding time.

The tip diameter of normal electrode was 6 mm. To investigate the effect of ETDE morphology on nugget shape and size, the sizes of upper and lower electrodes were different. The upper electrode was normal, and the lower electrode tip diameter increased from 7 to 10 mm at interval of 1 mm. In the same way, the upper electrode was normal and the lower electrode was pitting electrode whose pitting diameter changed from 1 to 3 mm at interval of 1 mm. Moreover, welding

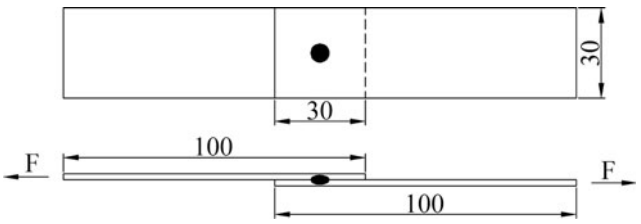

Fig. 3 Tensile-shear test sample

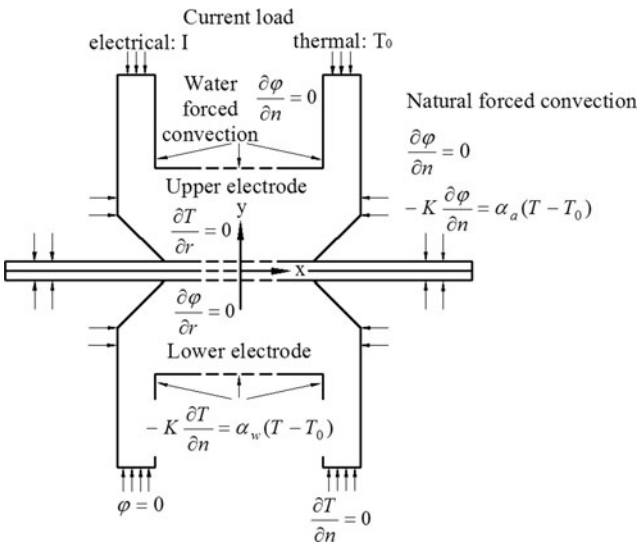

Fig. 4 Boundary conditions

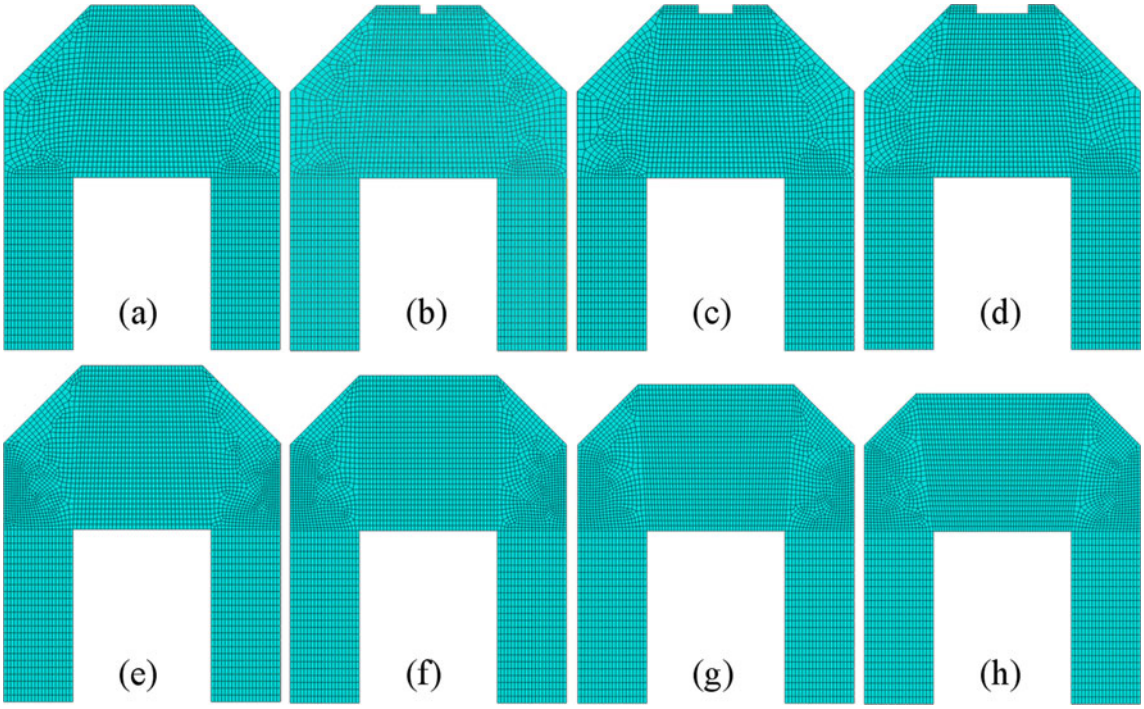

Fig. 5 Electrode tip morphologies in FE model: **a** normal, **b** EP-1 mm, **c** EP-2 mm, **d** EP-3 mm, **e** ETDE-7 mm, **f** ETDE-8 mm, **g** ETDE-9 mm, and **h** ETDE-10 mm

parameters of different electrode tip morphologies stayed the same. On the other hand, nugget shape and size were measured on the metallographic cross sections of the welds. All of the sectioned samples were ground, polished, and etched by 4 % nital reagent. XP-201 Nikon eclipse polarization microscope was used to investigate the effects of electrode tip morphology on nugget shape and size.

In addition, the static tensile-shear tests were carried out on the Instron1341 testing machine at a cross head speed of 10 mm/min, according to GB/T 2561-2008 [18]. The samples were prepared according to AWS standard [19] and are shown in Fig. 3. The lap shear fracture load (LSFL) and failure mode were measured during the tests.

3 FE modeling

A 2D fully coupled thermal-electrical model is proposed to predict nugget shape and size under ABAQUS software environment. The applied electrical and thermal boundary conditions are displayed in Fig. 4, where T_0 is the initial temperature, α_a is the air heat convection coefficient, α_w is the water heat convection coefficient, and n is the normal direction. What is more, the transient heat transfer and electric transfer equations are given by Moshayedi and Sattari-Far [20]:

$$\rho c\frac{\partial T}{\partial t}=\frac{1}{r}\frac{\partial}{\partial r}\left(Kr\frac{\partial T}{\partial r}\right)+\frac{1}{r}\frac{\partial}{\partial z}\left(Kr\frac{\partial T}{\partial z}\right)+Q \tag{3}$$

Table 3 Material properties of DP590 and copper alloy

Temperature (°C)		Thermal conductivity (w/m °C)		Electrical resistivity (Ω m×10^{-8})		Specific heat (J/kg °C)		Density (kg/m^3)	
WMP	EMP	WMP	EMP	WMP	EMP	WMP	EMP	WMP	EMP
25	21	65.3	64.75	28.4	14.2	460	397.8		
100	93	54.9	63.25	33.5	18.6	485	401.9		
200	204	45.2	55.33	40.2	26.7	519	418.7		
300	316	36.4	49.94	47.8	37.6	552	431.2		
400	427	28.5	44.86	56.4	49.5	586	439.6	7826	8900
500	649		34.91	66.6	81.8		452.2		
600	760		30.50	80.6	101.1		464.7		
700	871		28.41		111.5		477.3		
800	1093		28.56		117.9		480		

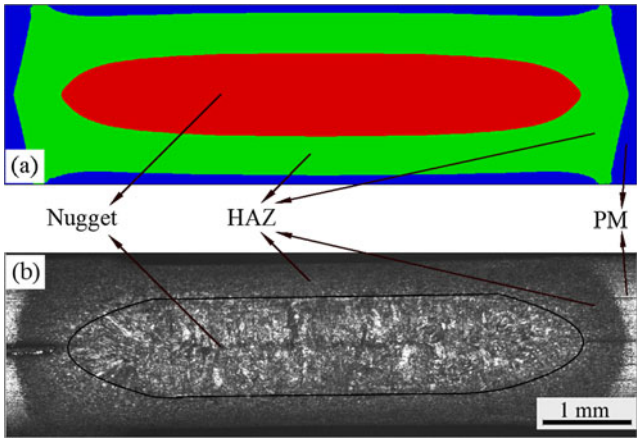

Fig. 6 Results of **a** simulation and **b** experiment

$$\frac{1}{r}\frac{\partial}{\partial r}\left(r\gamma\frac{\partial\varphi}{\partial r}\right)+\frac{\partial}{\partial z}\left(r\frac{\partial\varphi}{\partial z}\right)=0 \tag{4}$$

where c, ρ, and K are the specific heat, density, and thermal conductivity, respectively. T is the temperature, γ is the electrical conductivity, and φ is the electrical potential.

As mentioned above, pitting diameter varies from 1 to 3 mm at interval of 1 mm, which is expressed as EP-1 mm to EP-3 mm in the following. Electrode tip diameter increases from 7 to 10 mm at interval of 1 mm, which is expressed as ETDE-7 mm to ETDE-10 mm in the following. The whole electrode tip morphologies in FE model are given in Fig. 5.

The FE modeling process can be described as follows: Firstly, the material of worksheet is selected as DP590 while the electrode is copper alloy, and the material properties of workpiece (WMP) and electrode (EMP) are derived from Wang et al. [21] and shown in Table 3. Afterward, each workpiece and electrode should be assigned an initial temperature, as well as heat transmission and thermal radiation constants. Furthermore, a current load is applied on the surface of the upper electrode while the electrical potential of lower electrode surface is zero. The contact resistance can be considered as a thin layer of elements with high resistivity, which contains the contact resistance of sheet/sheet and sheet/electrode [14]. Finally, the worksheets and the electrodes are meshed using

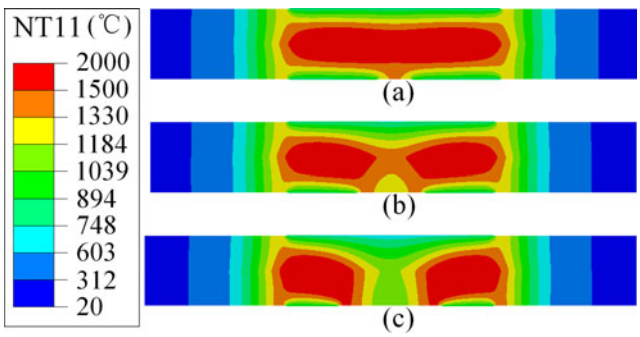

Fig. 7 Temperature distribution and nugget shape of different EP morphologies: **a** EP-1 mm, **b** EP-2 mm, and **c** EP-3 mm

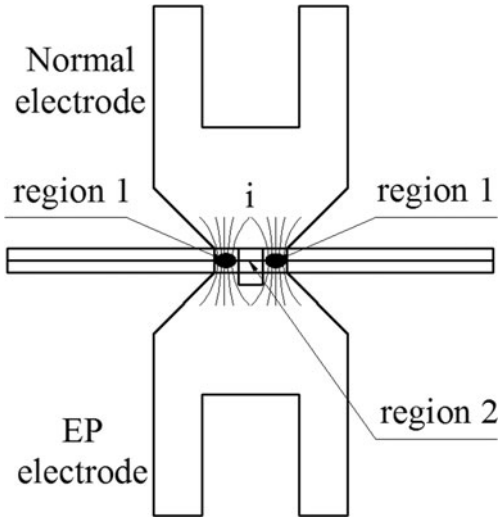

Fig. 8 EP condition

arbitrary Lagrangian-Eulerian (ALE) adaptive mesh method. This is effective to eliminate excessive element distortion which could lead to premature termination of the problem in cases involving large deformations. The element type is a four-node linear coupled thermal-electrical quadrilateral (C2D4E).

4 Results and discussions

4.1 Experimental verification of FE model

A normal RSW process is conducted in both simulation and experiment. According to the iron-carbon equilibrium diagram, 1500 degrees Celsius (°C) is considered as the melting temperature of DP590 steel, as demonstrated by Wan et al. [22]. That is, temperature zone higher than 1500 °C is regarded as nugget in the simulation.

The results of simulation and experiment are shown in Fig. 6. Considering 1500 °C as the melting temperature, nugget region is displayed as red color. Meanwhile, heat-affected zone (HAZ) and parent metal (PM) are respectively expressed

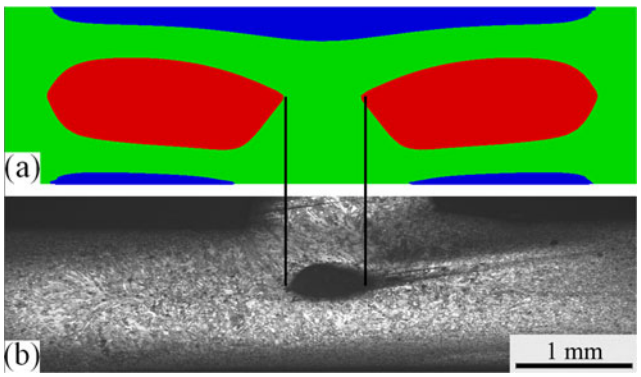

Fig. 9 EP-3 mm results of **a** simulation and **b** experiment

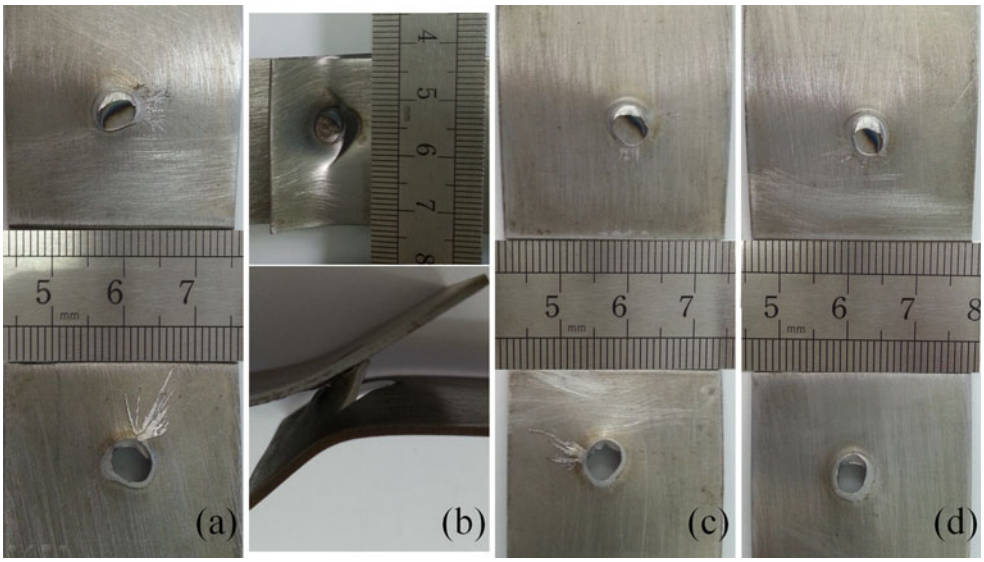

Fig. 10 Failure modes of different EP morphologies: **a** normal, **b** EP-1 mm, **c** EP-2 mm, and **d** EP-3 mm

as green color and blue color. Nugget section shape seems like a flat ellipse. In general, the major axis of the ellipse donates the nugget diameter and minor axis of the ellipse represents the nugget depth. The results show that nugget diameters of simulation and experiment are 5.35 and 5.381 mm, respectively. The nugget depths of simulation and experiment are 1.01 and 0.988 mm, respectively. The relative errors of nugget diameter and nugget depth are both less than 5 %. A good agreement is observed between the simulation and the experiment, and consequently, the FE model is reliable.

4.2 Effects of EP morphology

4.2.1 Nugget shape and size

The temperature distribution and nugget shape of different EP morphologies are shown in Fig. 7. It can be seen that nugget section shape seems like a pair of glasses due to incomplete fusion at the center of the workpieces' faying surface. And, increasing the pitting diameter of electrode extends the area of incomplete fusion zone. A little current flows through the center of the workpieces' faying surface because two workpieces are in the contact state in the initial welding stage, and the thermal expansion in the center (region 2) is not as significant as that in the periphery (region 1), resulting in center contact material separation. And then, there is no current flowing through the region 2, as demonstrated in Fig. 8. In the region 2, temperature growth mainly comes from heat conduction of region 1 because of the great temperature gradient between these two regions. With decreasing areas of region 1 due to increasing pitting diameter, heat conduction from region 1 to region 2 reduces, so that the heat of region 2 is not enough to melt this part of material, resulting in incomplete fusion and glass-section-shaped nugget.

The incomplete fusion diameters of EP-1, EP-2, and EP-3 mm are 0, 0.85, and 2.15 mm, respectively. That is to say, there is no incomplete fusion zone under the condition of a little EP. But, obvious EP will increase the incomplete fusion diameter. Enlargement of pitting diameter contributes to the increasing area of region 2 and decreasing area of region 1, and more heat dispersion hinders nugget growth, resulting in the

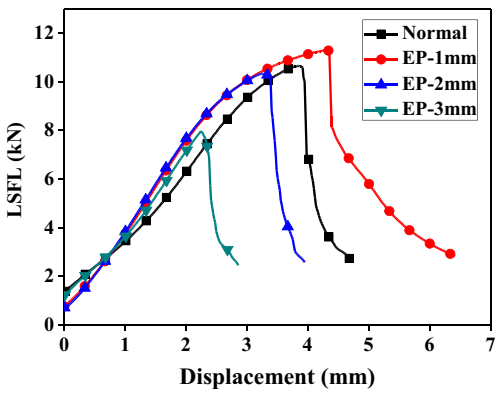

Fig. 11 LSFL-displacement curves of different EP morphologies

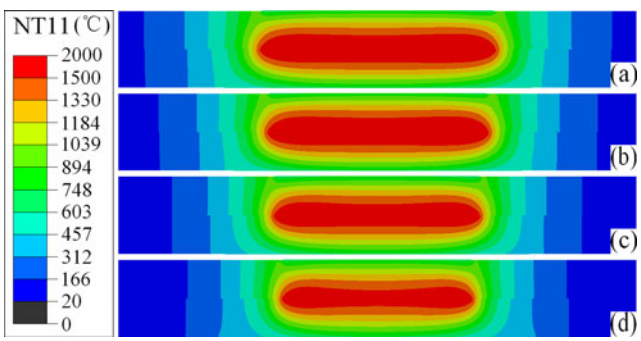

Fig. 12 Temperature distribution and nugget shape of different ETDE morphologies: **a** ETDE-7 mm, **b** ETDE-8 mm, **c** ETDE-9 mm, and **d** ETDE-10 mm

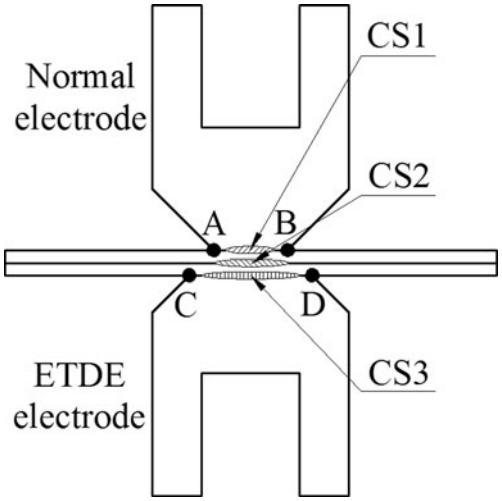

Fig. 13 ETDE condition

increasement of incomplete fusion diameter. The results of simulation and experiment of EP-2 mm are selected to verify the FE model, which are shown in Fig. 9. It can be seen that incomplete fusion diameters of simulation and experiment are, respectively, 0.85 and 0.801 mm, and the relative error is 6.12 %.

4.2.2 Failure behaviors

The test results of tensile-shear failure modes of different EP morphologies are displayed in Fig. 10. It can be seen that all of failure modes of different EP morphologies are pullout failure (PF) modes. Tensile stress at the circumference of the nugget is more effective than shear stress at the contact surface of sheet/sheet. The PF mode is a double-thickness failure, which occurs in both two overlapped metal sheets [23]. Tensile stress at the circumference of the nugget is the inducement for the PF mode. Lower hardness of PM than that of nugget and HAZ contributes to the formation for fracturing, and consequently, the ductile fracture happens at PM, as illustrated by Kaya and Kahraman [24].

Figure 11 shows the LSFL-displacement curves of different EP morphologies. Compared with the normal electrode, a higher load capacity [25] is needed when an electrode is under

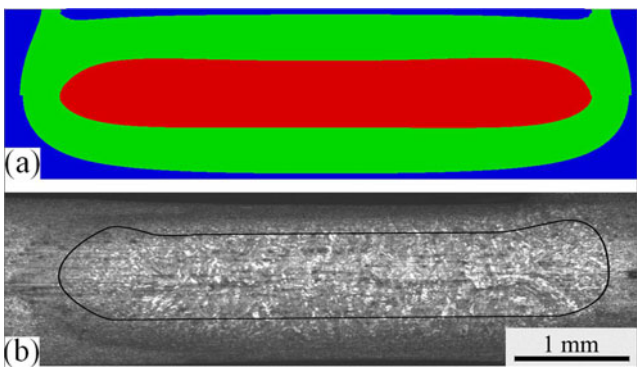

Fig. 14 ETDE-8-mm results of **a** simulation and **b** experiment

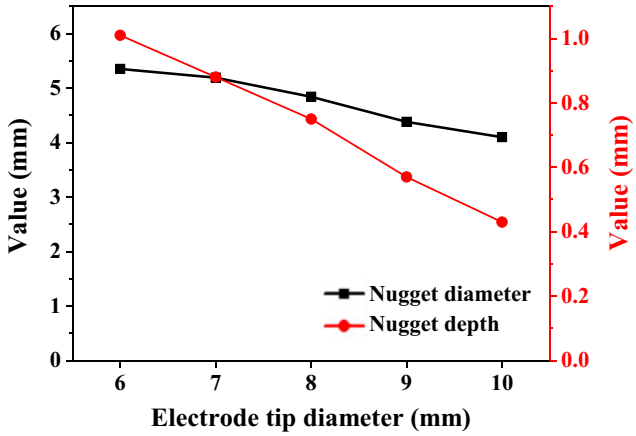

Fig. 15 Nugget sizes of different ETDE morphologies

a 1-mm pitting diameter; this is because there is no incomplete fusion zone and the nugget diameter enlarges slightly when the EP diameter is 1 mm. When the EP diameter is greater than 1 mm, the load capacity and energy absorption decrease with the increasing of EP diameter. It can be seen that the fracture loads of normal, EP-1, EP-2, EP-3 mm are 10.63, 11.29, 10.33, and 7.93 kN, respectively. Generally speaking, the fracture load reduces while the EP diameter enlarges due to the increasing area of incomplete fusion. When EP diameter is larger than 2 mm, the LSFL drops rapidly with increasing the pitting diameter. The fracture load of EP-3 mm is less than 75 % of the normal, taking 80 % of the normal LSFL as the criteria of the electrode degradation; the electrodes whose pitting diameter is over 3 mm can be regarded as the invalid electrodes.

4.3 Effects of ETDE morphology

4.3.1 Nugget shape and size

There are four cases whose electrode tip diameter varies from 7 to 10 mm at interval of 1 mm; temperature distribution and nugget shape of different ETDE morphologies are displayed in Fig. 12. It is obvious that nugget section shape seems like a hump. Taking CS1, CS2, and CS3 as the contact surface of upper electrode/sheet, sheet/sheet, and lower electrode/sheet, respectively, the different contact areas of CS1 and CS3 lead to the different current density distribution of them and then change the symmetry of temperature distribution in axial direction. In addition, current density at the edge of contact region is larger due to the edge effect, which promotes the appearance of large current sharp corners A, B, C, and D in Fig. 13. In general, the current density of CS1 is larger than that of CS3, which causes the current intensity of A and B to be larger than that of C and D, further leading to more heat generation. It contributes to the moving up of nugget edge (i.e., nugget edge moves to the direction of upper electrode), resulting in the formation of hump-section-shaped nugget.

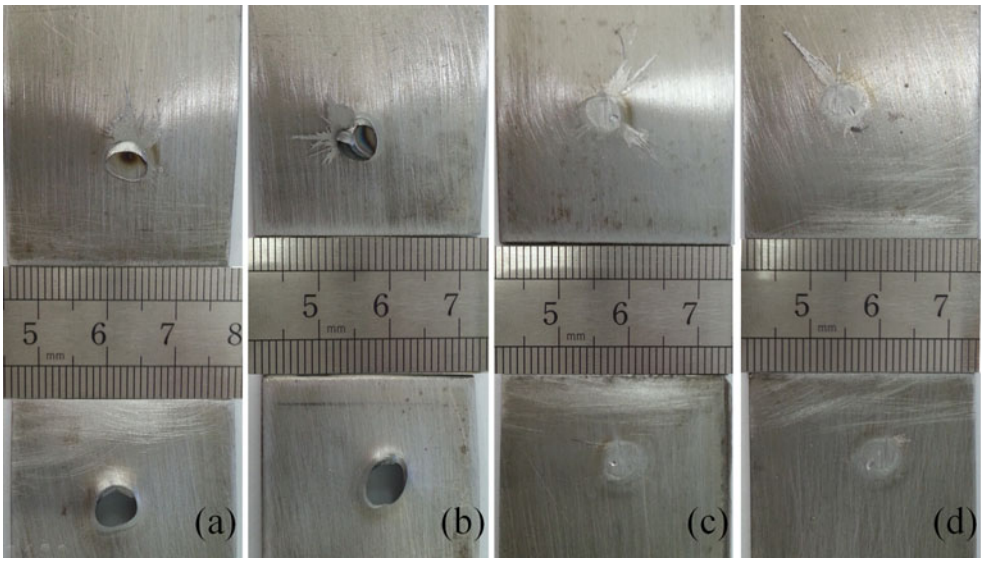

Fig. 16 Failure modes of different ETDE morphologies: **a** ETDE-7 mm, **b** ETDE-8 mm, **c** ETDE-9 mm, and **d** ETDE-10 mm

The results of simulation and experiment of ETDE-8 mm are selected to verify the FE model, which are shown in Fig. 14. It can be seen that the nugget diameters of simulation and experiment are 4.84 and 4.799 mm, respectively. The nugget depths of simulation and experiment are 0.75 and 0.741 mm, respectively. The relative errors of nugget diameter and nugget depth are both less than 5 %.

The nugget sizes of different ETDE morphologies are presented in Fig. 15. It can be seen that both of the nugget diameter and nugget depth reduce with the increasing of electrode tip diameter. Under the same welding condition, ETDE could decrease the current density, further reducing the generated heat. The temperature growth declines with the enlargement of electrode tip diameter, resulting in the nugget diameter and nugget depth reducing. In addition, the rate of nugget depth reduction is faster than that of nugget diameter reduction with the increasing of electrode tip diameter. This is because the heat dissipation condition in the axial direction is better than that of the radial direction under the different contact of electrode.

4.3.2 Failure behaviors

Failure modes obtained from the tensile-shear tests are diverse under different ETDE morphologies, as shown in Fig. 16. It can be seen that failure modes of ETDE-7 mm and ETDE-8 mm are both PF modes described above, and the failure modes of ETDE-9 mm and ETDE-10 mm are the interfacial failure (IF) modes, as presented in Fig. 16a–d. The IF mode is caused by the brittle fracture of weld nugget, and its fracture surface is relatively smooth and lustrous, as shown by Pouranvari [26]. Sheer stress at contact surface of sheet/sheet is the inducement for the IF mode, as stated by Dancette et al. [27], which depends on the size of nugget. With the increasing of electrode tip diameter, both of the nugget diameter and nugget depth decrease. Thus, stress concentrates on the edge of nugget and leads to the appearance of a small gap, and because of the rapid reduction of nugget depth, shear resistance of the nugget along its center line declines sharply. Therefore, the small gap extents and forms cracks; afterward, the cracks propagate along the center line of thin nugget and penetrate the whole nugget. In a word, the failure mode transmits from PF mode to IF mode with increasing the electrode tip diameter.

The LSFL-displacement curves of different EP morphologies are shown in Fig. 17. There is a difference between the LSFL-displacement curves of PF mode and IF mode. After reaching peak load, the load of IF mode drops faster than that of PF mode, which appears a linear decline trend. And, more displacement of the loading process is needed in PF mode than that of IF mode. It can be known that the fracture load of PF mode is greater than that of IF mode, which indicates that the welding quality of PF sample is superior to IF sample, as discussed by Charde et al. [28]. In addition, the fracture loads of ETDE-7 mm, ETDE-8 mm, ETDE-9 mm, and ETDE-10 mm are 10.49, 10.01, 8.56, and 7.50 kN,

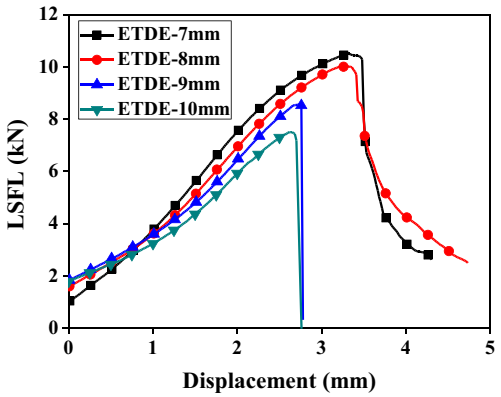

Fig. 17 LSFL-displacement curves of different ETDE morphologies

respectively. That is to say, the larger the electrode tip diameter is, the lower the LSFL is. Generally, nugget size determines welding quality; nugget diameter and nugget depth reduce when electrode tip diameter enlarges, resulting in the decline of LSFL. According the failure criteria of the electrode, the electrodes whose tip diameter is over 9 mm are the invalid electrodes.

5 Conclusions

In this paper, the effects of EP and ETDE morphologies on RSW quality of DP590 steel are investigated using FE and experimental methods. Simulation illustrates the nugget shape and size, which is verified by experimental data. Failure mode and LSFL are obtained from experimental tests. The main results can be drawn as follows:

1. Ellipse-section-shaped nugget is developed under the normal RSW condition, while glass-section-shaped nugget under the EP condition and hump-section-shaped nugget under the ETDE condition, respectively.
2. A little EP enlarges the LSFL slightly, and there is no incomplete fusion zone under this condition. But, obvious EP will reduce the LSFL, and the incomplete fusion diameter increases with the increasing of EP diameter.
3. All of the nugget diameter, nugget depth, and LSFL decrease when the electrode tip diameter increases.
4. Failure modes of different EP morphologies are the PF mode, which vary from IF mode to PF mode with increasing electrode tip diameter.

Acknowledgments This work was supported by the National 863 Program (No. 2013AA040201), the Innovative Research Team Development Program of Ministry of Education of China (No. IRT13087), the High-end Talent Leading Program of Hubei Province (No. 2012-86), and the Science and Technology Support Program of Hubei province (No. 2015BCE083).

References

1. Yang HG, Liu XM, Zhang YS, Chen GL (2010) Investigations on the weldability of high-strength steels sheet to cylindrical tube single-sided spot welding. Int J Adv Manuf Technol 49:513–518
2. Mohsen E, Mark AT, Mohsen AZ, Sergio D (2014) Effect of resistance spot welding parameters on weld pool properties in a DP600 dual-phase steel: a parametric study using thermomechanically-coupled finite element analysis. Mater Des 56:387–397
3. Hayat F, Sevim İ (2012) The effect of welding parameters on fracture toughness of resistance spot-welded galvanized DP600 automotive steel sheets. Int J Adv Manuf Technol 58:1043–1050
4. Zhang HQ, Qiu XM, Xing F, Bai J, Chen JH (2014) Failure analysis of dissimilar thickness resistance spot welded joints in dual-phase steels during tensile shear test. Mater Des 55:366–372
5. Holliday R, Parker JD (1995) Electrode deformation when spot welding coated steels. Weld World 35(3):160–166
6. Fukumoto S, Lum I, Biro E, Boomer DR (2003) Effects of electrode degradation on electrode life in resistance spot welding of aluminum alloy 5182. Weld J 82(11):307s–312s
7. Zhang XQ, Chen GL, Zhang YS (2008) Characteristics of electrode wear in resistance spot welding dual-phase steels. Mater Des 29: 279–283
8. Wang YR, Feng JC, Zhang ZD (2005) Effect of electrode wear on weld nugget formation in resistance spot welding of magnesium alloy. Trans Nonferrous Metals Soc China 15(3):327–330
9. Holliday R, Parker JD, Williams NT (1996) Predication of electrode campaign life when spot welding zinc coated steels incorporating electrode tip dressing operations. Ironmak Steelmak 23(2):157
10. Lum L, Fukumoto S, Biro E, Boomer DR, Zhou Y (2004) Electrode pitting in resistance spot welding of aluminum alloy 5182. Metall Mater Trans A 35A:217–226
11. Khan JA, Xu L, Chao YJ (1999) Prediction of nugget development during resistance spot welding using coupled thermal–electrical–mechanical model. Sci Technol Weld Join 4(4):201–207
12. Xu L, Khan JA (1999) Nugget growth model for aluminum alloys during resistance spot welding. Weld Res Suppl 78(11):367–372
13. Nodeh IR, Serajzadeh S, Kokabi AH (2008) Simulation of welding residual stresses in resistance spot welding, FE modeling and X-ray verification. J Mater Process Technol 205:60–69
14. Karimi MR, Sedighi M, Afshari D (2015) Thermal contact conductance effect in modeling of resistance spot welding process of aluminum alloy 6061-T6. Int J Adv Manuf Technol 77:885–895
15. Ma NS, Murakawa H (2010) Numerical and experimental study on nugget formation in resistance spot welding for three pieces of high strength steel sheets. J Mater Process Technol 210:2045–2052
16. Zou JS, Zhao QZ, Chen Z (2009) Surface modified long-life electrode for resistance spot welding of Zn-coated steel. J Mater Process Technol 209:4141–4146
17. Dong SJ, Zhou N, Cheng CK, Shi YW, Chang BH (2005) Electrode degradation mechanism during resistance spot welding of zinc coated steel using Cu-TiB_2 electrodes. Trans Nonferrous Metals Soc China 15(6):1219–1225
18. GB/T 2651-2008/ISO 4136: 2001 (2008) Tensile test method on welded joints. Standardization administration of the People's Republic of China
19. Recommended practices for test methods and evaluation the resistance spot welding behavior of automotive sheet steels, ANSI/AWS/SAE D8.9-97
20. Moshayedi H, Sattari-Far I (2012) Numerical and experimental study of nugget size growth in resistance spot welding of austenitic stainless steels. J Mater Process Technol 212:347–354
21. Wang M, Zhang HD, Pan H, Lei M (2009) Numerical simulation of nugget formation in resistance spot welding of DP590 dual-phase Steel (in Chinese). J Shanghai Jiaotong Univ 43(1):56–60
22. Wan XD, Wang YX, Zhang P (2014) Modeling the effect of welding current on resistance spot welding of DP600 steel. J Mater Process Technol 214:2723–2729
23. Pouranvari M, Marishi SPH (2010) On the failure of low carbon steel resistance spot welds in quasi-static tensile-shear loading. Mater Des 31:3647–3652
24. Kaya Y, Kahraman N (2012) The effects of electrode force, welding current and welding time on the resistance spot weldability of pure titanium. Int J Adv Manuf Technol 60:127–134
25. Sun X, Khaleel MA (2007) Dynamic strength evaluations for self-piercing rivets and resistance spot welds joining similar and dissimilar metals. Int J Impact Eng 34:1668–1682

26. Pouranvari M (2012) Susceptibility to interfacial failure mode in similar and dissimilar resistance spot welds of DP600 dual phase steel and low carbon steel during cross-tension and tensile-shear loading conditions. Mater Sci Eng A 546:129–138
27. Dancette S, Fabrègue D, Massardier V, Merlin J, Dupuy T, Bouzekri M (2011) Experimental and modeling investigation of the failure resistance of advanced high strength steels spot welds. Eng Fract Mech 78:2259–2272
28. Charde N, Yusof F, Rajkumar R (2014) Material characterizations of mild steels, stainless steels, and both steel mixed joints under resistance spot welding (2-mm sheets). Int J Adv Manuf Technol 75:373–384